Available online at www.sciencedirect.com

jmr&t Journal of Materials Research and Technology

journal homepage: www.elsevier.com/locate/jmrt

Original Article

Application of various fractal models in characterizing the morphology of pore structures of hydrating cement pastes

Jiyoung Kim [a,b], *Geuntae Hong* [a,c], *Sangwoo Oh* [a], *Seongcheol Choi* [a,*]

[a] *Department of Civil and Environmental Engineering, Chung-Ang University, 84 Heukseok-ro, Dongjak-gu, Seoul 06974, South Korea*

[b] *Structural Engineering Research Institute, Korea Institute of Civil Engineering and Building Technology, 283 Goyangdae-ro, Ilsanseo-gu, Goyang-si, Gyeonggi-do 10223, South Korea*

[c] *Department of Civil Engineering, Kyungpook National University, 80 Daehak-ro, Buk-gu, Daegu 41566, South Korea*

ARTICLE INFO

Article history:
Received 23 May 2022
Accepted 24 August 2022
Available online 31 August 2022

Keywords:
Fractal concept
Geometric perspective
Hydration
Pore structure
Sorptivity

ABSTRACT

The pore structures of cementitious materials are very crucial to the development of the various engineering properties of these materials. Based on the importance of the pore structure, several studies have been conducted on the application of fractal geometry, which can be used as an interpretation tool for the characteristics of the pore structure as well as in various engineering phenomena. Accordingly, various fractal models have been developed from the mercury intrusion porosimetry (MIP) data. However, studies on applying the fractal model considering the characteristics of the material to be analyzed are relatively scarce. In this study, we conducted an in-depth investigation of the characteristics of the pore structures of cementitious materials considering both the volumetric and geometric characterization parameters. Among the three concepts of fractal dimensions of pore-size distribution, the solid mass fractal concept exhibited the highest correlation with the degree of hydration. The fractal dimensions of pore-size distribution and pore tortuousness tended to increase as the complexity of the entire microstructures increased, mainly due to the increase in the solid phase fraction. Furthermore, the results of the correlation analysis (between the volumetric and geometric parameters) and regression analysis (between newly derived parameter and initial sorptivity) showed that fractal dimensions can be utilized as pore structure characterization parameters like the existing volumetric parameters, and these parameters serve as complementary tools for interpreting the transport properties of cementitious materials.

* Corresponding author.
E-mail address: schoi@cau.ac.kr (S. Choi).

https://doi.org/10.1016/j.jmrt.2022.08.122

1. Introduction

Cementitious materials, such as cement paste, cement mortar and concrete, are porous media that consist of microstructures including hydration products, unhydrated cement particles and pores. Unlike other porous media, cementitious materials have the characteristic that their microstructures change continuously as the hydration proceeds. In the microstructure, the part of the assembly of pore phases other than the solid phases is the pore structure. Thus, the changes in the pore structure are caused by the changes in the microstructure due to the hydration, and these changes have a significant effect on the development of various mechanical properties and the durability of concrete, such as strength, permeation, diffusion, shrinkage, and freeze-thaw [1–5]. Accordingly, the characteristics of the microscopic pore structure act as important factors in determining the performance of concrete. To accurately interpret the various engineering properties of concrete, it is necessary to continuously develop the techniques that can analyze the characteristics of the pore structure more realistically.

Currently, the pore structure can be measured directly using experimental techniques, such as nuclear magnetic resonance [6], nitrogen adsorption/desorption [7] and mercury intrusion porosimetry (MIP) [8], or predicted indirectly by computer-based models, such as HYMOSTRUC [9] and CEMHYD3D [10]. In the most of the pore structure analysis techniques through existing experiments and computer-based models as mentioned above, the characteristics of the pore structure are mainly evaluated by volumetric characterization parameters, such as the size, area, volume of pores and porosity. However, the actual pore structure of the cementitious material is considered as chaotic system with highly complex structure because they also have geometric characteristics that are difficult to quantify, such as a wide pore-size range, irregular pore shapes and disorderly pore spatial distributions [11–13]. Even if the pore structure has similar volumetric characterization parameters, different geometric characteristics may appear, thus making it difficult to clearly analyze the characteristics of the actual pore structure using only the volumetric characterization parameters [14,15]. Therefore, for a clearer analysis of the pore structure, there is a need for a reliable expression that can reflect the geometrical aspects of the pore structure. In this regard, the connectivity of the pores, effective porosity, pore-size distribution, critical and threshold pore diameters are already used as the parameters that can reflect the complex morphology of the pore structure. However, these parameters are still expressed in a volumetric manner.

The actual morphology of the porous microstructure is more complicated than the common shape expressed in integer dimensions, such as a point, line, plane and space defined in the Euclidean geometry. To evaluate the realistic geometrical characteristics of such a structure, fractal geometry was introduced in the late 1970s by Mandelbrot [16]. According to the fractal geometry, a structure having the characteristics of self-similarity and recursiveness, in which a small part of a structure is similar to the whole structure and repeats within a certain scale, can be regarded as a fractal structure [17]. Although the fractal structure is comprised of a structurally complex-patterned and chaotic system, it can be quantified as a non-integer fractal dimension through theoretical expressions. Therefore, complex geometric characteristics of the pore structure within the porous microstructure can be quantitatively evaluated through non-integer fractal dimensions [18]. The pore structure of a cementitious material is formed in a geometrically complicated shape by a series of binder hydration processes [19], and this is the fractal structure with obvious fractal characteristics in terms of the pore-size distribution and tortuousness of the connected pore paths, as previous studies have shown [20–28]. Therefore, if the pore structure is analyzed using the geometric characterization parameters of fractal dimensions together with the existing volumetric characterization parameters, the complex pore structure can be analyzed more effectively, as the two types of parameters act complementarily.

Based on the necessity for fractal geometry, various fractal models for quantifying geometric characteristics in terms of the pore-size distribution and tortuousness of the pore paths have been developed by existing studies [21,29–33]. Among them, the models developed to describe the geometric characteristics in terms of the pore-size distribution are generally classified into three concepts based on theoretical principles: pore surface fractal [21,29], pore mass fractal [30] and solid mass fractal [31]. These three concepts of fractal models describe the pore-size distribution characteristics of the microstructure in three aspects: pore surface, pore volume and solid volume, respectively [34]. However, to date, these models have been used differently by different researchers without considering the intrinsic properties of the materials to be analyzed. For cementitious materials, hydration is the intrinsic property. The hydration of cementitious materials causes the variation in morphological characteristics of the microstructures, which are consisted of pore phases, solid phases and the interface of these two phases. Even under the same hydration mechanism, the ranges of the fractal dimensions may vary depending on the aspect from which the changes in the geometric characteristics of the microstructures are analyzed. Due to this, the results of each study vary widely, and a comparison of the results of each study is likely to be ambiguous, which limits progress in the related research [34]. Therefore, in order to attain individual results and to make possible comparisons with other results from studies dealing with various cementitious materials, it is necessary to determine the representative fractal concept suitable for analyzing the pore structure of the cementitious material. Moreover, studies based on such consideration of material properties are essential for practical uses.

Consequently, the main aim of this study was to conduct an in-depth investigation on the characteristics of the pore structures of cement pastes in geometric aspects. To this end, the porosimetric characteristics of cement paste specimens with water-to-cement (w/c) ratios of 0.3, 0.4 and 0.5 were measured at the ages of 1, 3, 7, 14 and 28 days using the MIP test. Due to the relatively simple and fast experimental procedure and the ability to measure the wider range of pore sizes than other pore structure evaluation techniques, this study used the MIP test. Based on the results of the MIP measurements, the fractal characteristics in terms of the pore-size

distribution were quantified and analyzed. Then, a comparative analysis between each fractal dimension, derived from the three concepts of fractal models, and the degree of hydration was conducted. By synthesizing the analysis results, the representative fractal concept suitable for cementitious materials was proposed. Furthermore, the fractal characteristics in terms of the pore tortuousness also quantified, and correlation analysis among the volumetric and geometric characterization parameters were conducted. Additionally, the initial sorptivity of the specimens were measured at the ages of 1, 3, 7, 14 and 28 days to verify the effectiveness of applying fractal geometry on interpreting the transport properties of the specimens. We expected that the results from this study will play a meaningful role in providing further and improved insights into the pore structures and engineering performances of cementitious materials.

2. Experimental methods

2.1. Materials and preparation of the specimens

Cement pastes with w/c of 0.3, 0.4 and 0.5 were fabricated using Type-I ordinary Portland cement (OPC, Sungshin Cement Co., Ltd. Korea). Table 1 shows the chemical composition of the cement. The specimen IDs were OPC 0.3, OPC 0.4 and OPC 0.5, depending on the mixture proportions. After the materials were mixed in accordance with ASTM C305-14 [35], the specimens were cast into cubic molds (50 × 50 × 50 mm) for the MIP test and cylindrical molds (100 mm in diameter and 200 mm in height) for the capillary water absorption test. Then, the fabricated specimens were cured for 24 h at 23 ± 1 °C and 100% RH condition. After 24 h of curing, the specimens were cured in water at 23 ± 1 °C for 1, 3, 7, 14 and 28 days.

2.2. Test methods

In this study, the MIP and capillary water absorption tests were conducted to analyze the variations in the pore structures by hydration and transport properties, respectively. The MIP test specimens were split into 10 × 10 × 10 mm cubes at the core position of the fabricated specimens at the ages of 1, 3, 7, 14 and 28 days. Then, the split specimens were immersed in acetone for 24 h to stop the hydration. Thereafter, the specimens were dried for 24 h in an oven at 105 °C to remove the residual water and acetone. In this study, oven drying at 105 °C, where drying occurs fast [36], was selected to prevent further hydration from the test date. In this case, the specimens dried at 105 °C is considered that only evaporable water was removed from the pores [37]. The MIP test was conducted using Micromeritics AutoPore V 9605 for the specimens after pretreatment. The specimens to be tested were placed in the penetrometer after measuring the weight. After the experiment started, mercury was injected into the specimens through the low- and high-pressure stages in which pressures were applied to the specimens step by step from 0.2 to 33,000 psia. The contact angle between the injected mercury and microstructure of the cement paste and the surface tension of mercury were 130° and 0.000485 N/mm, respectively. The minimum pore diameter that could be measured via the maximum mercury injection pressure of 33,000 psia was approximately 5.5 nm.

The capillary water absorption test was conducted in accordance with the modified ASTM C1585-13 [38]. Fig. 1 shows the experimental setup. At specific curing ages, specimens of 100 mm in diameter and 25 mm in height were cut from the middle of the fabricated cylindrical specimens. The cut specimens were dried in an oven at a temperature of 105 °C for 3 days until a constant mass was obtained (variation below 0.5%). Then, the side and top surfaces of the specimens were sealed with an aluminum foil tape to prevent water evaporation. Thereafter, the original masses of the sealed specimens were measured before starting the test. The specimens were placed on the specimen supports, and the water level was maintained at approximately 3 mm above the bottom of the specimens. After immersion, the masses of the specimens were recorded at regular time intervals of 1, 5, 10, 20, 30 and 60 min, and every hour up to 6 h. The initial sorptivity can be determined from 1 min to 6 h according to:

$$I = \frac{\Delta W}{A \cdot \rho} = S \cdot t^{1/2} + I_0 \quad (1)$$

where I denotes the water absorption, ΔW denotes the mass of absorbed water, A denotes the area of the specimen exposed to water, ρ denotes the water density, S denotes the sorptivity, t denotes the time, and I_0 denotes the correction term added for describing the surface effects that occurs when the specimen comes in contact with water [39].

3. Methodology for evaluating fractal characteristics of pore structure

3.1. Fractal characteristics of pore-size distribution

The geometric characteristics of the pore-size distribution within the pore structure are mainly characterized by using the concept of mass fractal and surface fractal. Mass fractal is subdivided into pore mass fractal and solid mass fractal. In the mass fractal concept, both the pore (or solid) itself and its surface or the interface with other materials are fractal. Mass fractal has the characteristic that the mass of pore (or solid) is surrounded by a sphere, and its geometrical characteristic changes in proportion to the power of the radius of that sphere

Table 1 – Chemical composition of the cement.

	SiO_2	Al_2O_3	Fe_2O_3	CaO	MgO	K_2O	Na_2O	SO_3	H_2O	LOI[a]	Sum
Cement (mass %)	20.80	4.93	3.50	62.40	1.61	0.90	0.33	2.21	–	2.74	99.42

[a] LOI: loss of ignition.

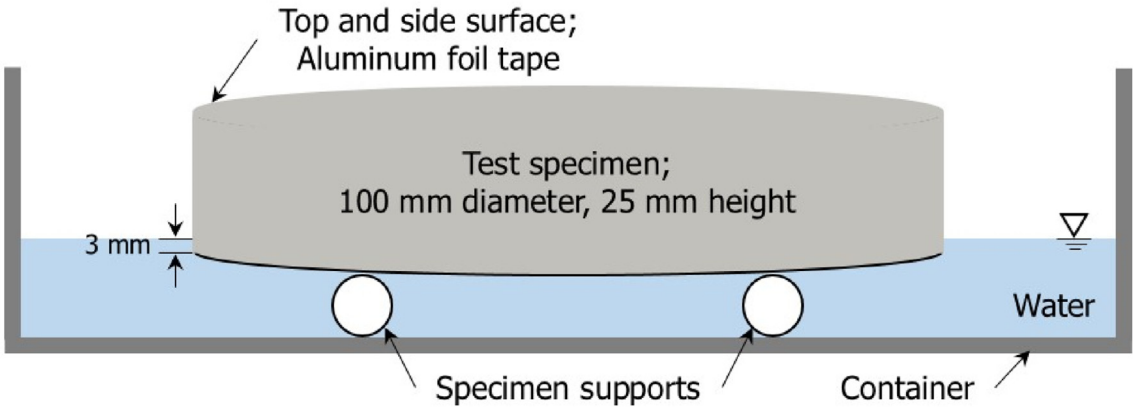

Fig. 1 – Schematic of the experimental setup for capillary water absorption test.

[37]. This power is the dimension of the mass fractal. In the surface fractal concept, a surface or an interface with other materials is fractal. If the fractal geometry is applied to a solid-pore system such as the microstructure of cement paste, the pore structure is essentially the inverse of the solid phase; therefore, the solid phase and pore structure share the same boundaries [37].

As described above, since the fractal concept used to analyze the geometric characteristics of the pore-size distribution is based on the information of the pore or solid phase, it is important to obtain information on the pore structures of the porous media as a first step. The pore structural characteristics of the porous media can be obtained through various experimental techniques or computer-based models, of which the MIP test is frequently used due to its easy implementation and wide range of size of measurable pores. To analyze the fractal characteristics of the pore-size distribution based on the porous microstructure data, various fractal models, developed by Pfeifer and Avnir [40], Usteri et al. [31], Zhang and Li [21], Neimark [41], Friesen and Mikula [29], Li [30] and Ji et al. [20], have been proposed so far. Among them, the fractal characteristics of the pore-size distribution were analyzed in this study using the models developed by Zhang and Li [21], Li [30] and Usteri et al. [31], derived based on the concept of pore surface fractal, pore mass fractal, and solid mass fractal, respectively.

As shown in Eq. (2), Zhang and Li [21] proposed a model for deriving the pore surface fractal dimension based on the law of conservation of energy between the increase in the pore surface energy due to mercury penetration and the work energy required for intruding mercury into the pores during the MIP test.

$$D_{f,PSF} \propto \frac{\log(W_n/r_n^2)}{\log(V_{p,n}^{1/3}/r_n)} \tag{2}$$

where $D_{f,PSF}$ denotes the pore surface fractal dimension, r_n denotes the pore radius at the mercury intrusion stage n, $V_{p,n}$ denotes the total mercury volume when mercury intrudes into the pores of r_n, and W_n denotes the cumulative surface energy during mercury intrusion, which is derived through:

$$W_n = \sum_{k=1}^{n} P_k \Delta V_{p,k} \tag{3}$$

where k denotes the mercury intrusion stage, P_k and $\Delta V_{p,k}$ denote the mercury intrusion pressure and the mercury intrusion volume at the stage k, respectively. The parameter $D_{f,PSF}$ is the slope of the $\log(V_{p,n}^{1/3}/r_n) - \log(W_n/r_n^2)$ curve, which characterizes the complexity of pore-size distribution through the roughness of the pore surface.

Under the assumption that the pore structures of the porous media consist of capillaries with the same lengths and

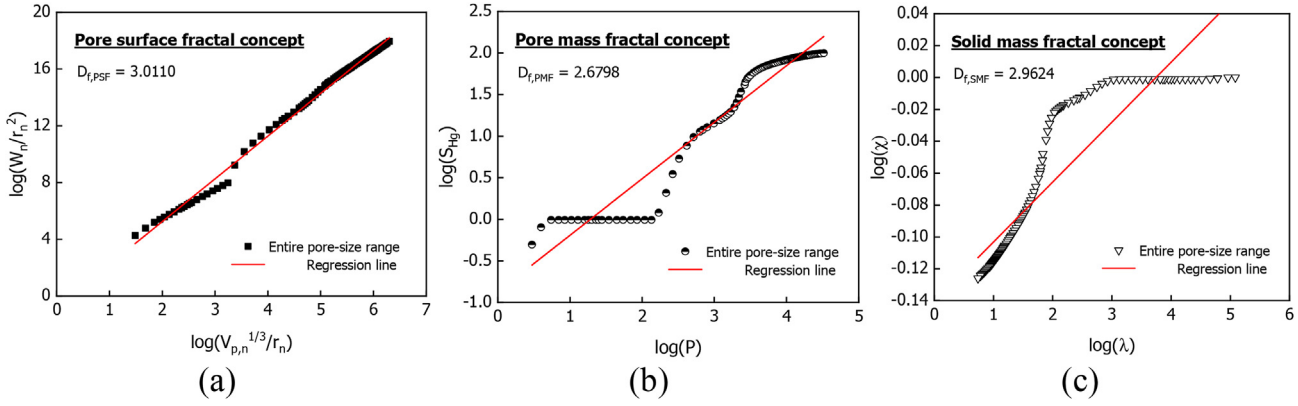

Fig. 2 – Logarithm plots of $\log(V_{p,n}^{1/3}/r_n) - \log(W_n/r_n^2)$, $\log(P) - \log(S_{Hg})$ and $\log(\lambda) - \log(\chi)$ for the entire pore-size range (OPC 0.3, one day data). (a) pore surface fractal concept; (b) pore mass fractal concept; and (c) solid mass fractal concept.

various radii [42], Li [30] developed the model based on packing the volume of capillaries having different radii and the relationship between the number of packing capillaries and pore radii, as follows:

$$\frac{V_{Hg}}{\pi r^2 l} \propto r^{-D_{f,PMF}} \tag{4}$$

where V_{Hg} denotes the cumulative volume of mercury that intrudes into the specimen, r denotes the pore radius, l denotes the length of capillary, and $D_{f,PMF}$ denotes the pore mass fractal dimension. Meanwhile, according to the Washburn equation, the capillary pressure P is inversely proportional to the pore radius; also, when mercury is intruded into the pore, the mercury saturation S_{Hg} in the pore structure is proportional to V_{Hg}. Thus, $D_{f,PMF}$ can be derived through the relationship between S_{Hg} and P, as follows:

$$S_{Hg} \propto P^{-(2-D_{f,PMF})} \tag{5}$$

In the Usteri et al. model [31], the solid mass fractal dimension is derived through the logarithmic relationship between the pore diameter and the fraction of solid volume to the total volume of porous microstructure, as follows:

$$\chi = \frac{V_t - V_p}{V_t} \tag{6}$$

$$D_{f,SMF} \propto 3 - \frac{\log(\chi)}{\log(\lambda)} \tag{7}$$

where χ denotes the solid fraction, V_t and V_p denote the total volume of the specimen and the cumulative pore volume, respectively, $D_{f,SMF}$ denotes the solid mass fractal dimension, and λ denotes the pore diameter. The parameter $D_{f,SMF}$ can be calculated by using the slope of the $\log(\lambda) - \log(\chi)$ curve, which characterizes the complexity of the pore-size distribution through the volume fraction of the solid phase.

As summarizing, the pore surface, pore mass and solid mass fractal dimension are calculated through the surface properties of the pore structure (i.e., roughness), pore volume and the fraction of the solid phase within the microstructure, respectively. In this study, based on the pore structure information obtained through the MIP test, the fractal dimensions of pore-size distribution of three concepts were derived through these control factors.

3.2. *Fractal characteristics of the tortuousness of the pore paths*

While various models for evaluating the fractal characteristics of the pore-size distribution have been proposed by various researchers, relatively little attention has been given to the study on the fractal characteristics of the tortuousness of the pore paths. In most studies, tortuosity was used to describe the tortuousness of the pore paths; however, the geometric characteristics of the tortuousness of the pore paths can be more clearly expressed through the fractal dimension of pore tortuousness [32,33]. According to the research of Wheatcraft and Tyler [43] and Yu and Cheng [44], the fractal scaling relation between the diameter and length of the capillary was developed as follows:

$$L_T(\lambda) = \lambda^{(1-D_T)} L_0^{D_T} \tag{8}$$

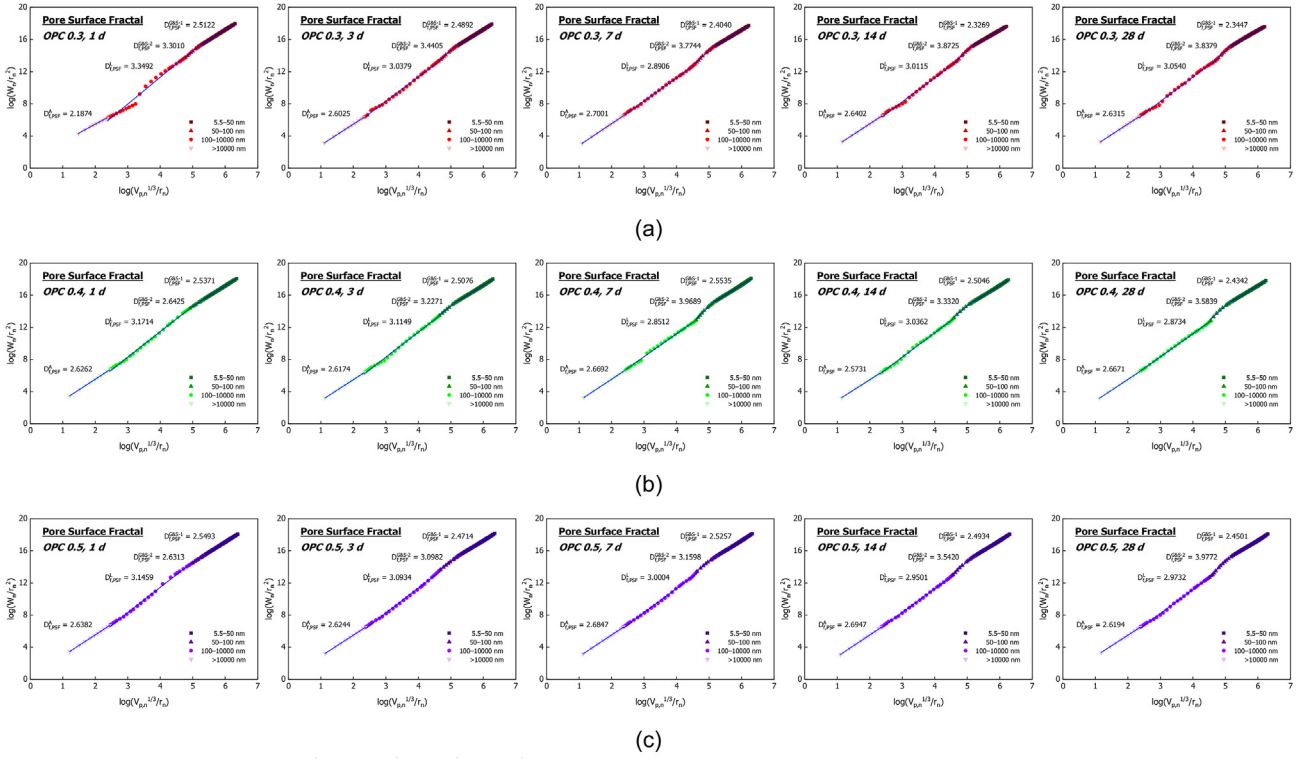

Fig. 3 – Logarithm plots of $\log(V_{p,n}{}^{1/3}/r_n) - \log(W_n/r_n{}^2)$ for the four pore-size ranges. (a) OPC 0.3; (b) OPC 0.4; and (c) OPC 0.5.

where D_T denotes the fractal dimension of pore tortuousness, L_0 denotes the straight-line length of the pore path (in this study, L_0 was estimated to be 10 mm under the assumption that a straight pore path as much as the height of the specimen exists within the MIP test specimen) and $L_T(\lambda)$ denotes the actual length of tortuous pore path with a diameter of λ. The tortuosity is the ratio of the actual tortuous length to the straight length of the pore path, expressed using the above Eq. (8).

$$\tau = \frac{L_T(\lambda)}{L_0} = \left(\frac{L_0}{\lambda}\right)^{D_T-1} \tag{9}$$

where τ denotes the tortuosity. Then, the fractal dimension of pore tortuousness can be expressed as follows:

$$D_T = 1 + \frac{\ln(\overline{\tau})}{\ln\left(L_0/\overline{\lambda}\right)} \tag{10}$$

where $\overline{\tau}$ denotes the average tortuosity and $\overline{\lambda}$ denotes the average pore diameter. In this study, the tortuosity of the pore paths was obtained via the geometry model proposed by Bo-Ming and Jian-Hua, as follows [45]:

$$\overline{\tau} = \frac{1}{2}\left[1 + \frac{1}{2}\sqrt{1-\varphi} + \sqrt{1-\varphi}\cdot\frac{\sqrt{\left(\frac{1}{\sqrt{1-\varphi}}-1\right)^2+\frac{1}{4}}}{1-\sqrt{1-\varphi}}\right] \tag{11}$$

where φ denotes the porosity. Eq. (11) was proposed based on the assumption that some capillaries overlap within the porous material and the others do not [45]. For cement pastes, solid hydrates are precipitated and accumulated on the surface of randomly distributed cement particles, and the pore network is formed as some hydrates fill the pore space. Of course, the idealized configuration of the porous medium proposed by Eq. (11) is not completely identical to the actual complex hydrated cement pastes in that it is a simple geometric model derived by arbitrarily averaging the possibility of overlapping particles, which are form of square. However, the tortuosity can be derived by directly utilizing the microstructural properties of the hydrated cement pastes without empirical constants, and in the previous study [46], when the tortuosity was calculated using other law, the results similar to those obtained through Eq. (11) were derived. In this regard, this study determined that the geometrical model of Eq. (11) can sufficiently evaluate the tortuous properties of the pore network of the hydrated cement pastes and utilized it.

The pores present within the microstructure of cement paste exist in the form of pore paths that are randomly distributed and connected to each other. Therefore, D_T plays an important role in determining the actual length of the pore paths, leading to a more accurate description of the actual pore structure.

4. Results and discussion

4.1. *Fractal dimension of pore-size distribution*

4.1.1. *Entire pore-size range*

Fig. 2(a)–(c) show the relationship of $\log(V_{p,n}{}^{1/3}/r_n) - \log(W_n/r_n{}^2)$, $\log(P) - \log(S_{Hg})$ and $\log(\lambda) - \log(\chi)$ for the entire pore-size range of the OPC 0.3 specimen at an age of one day, respectively. In the graphs, subscripts f,PSF, f,PMF and f,SMF represent the concept of the pore surface fractal, pore mass

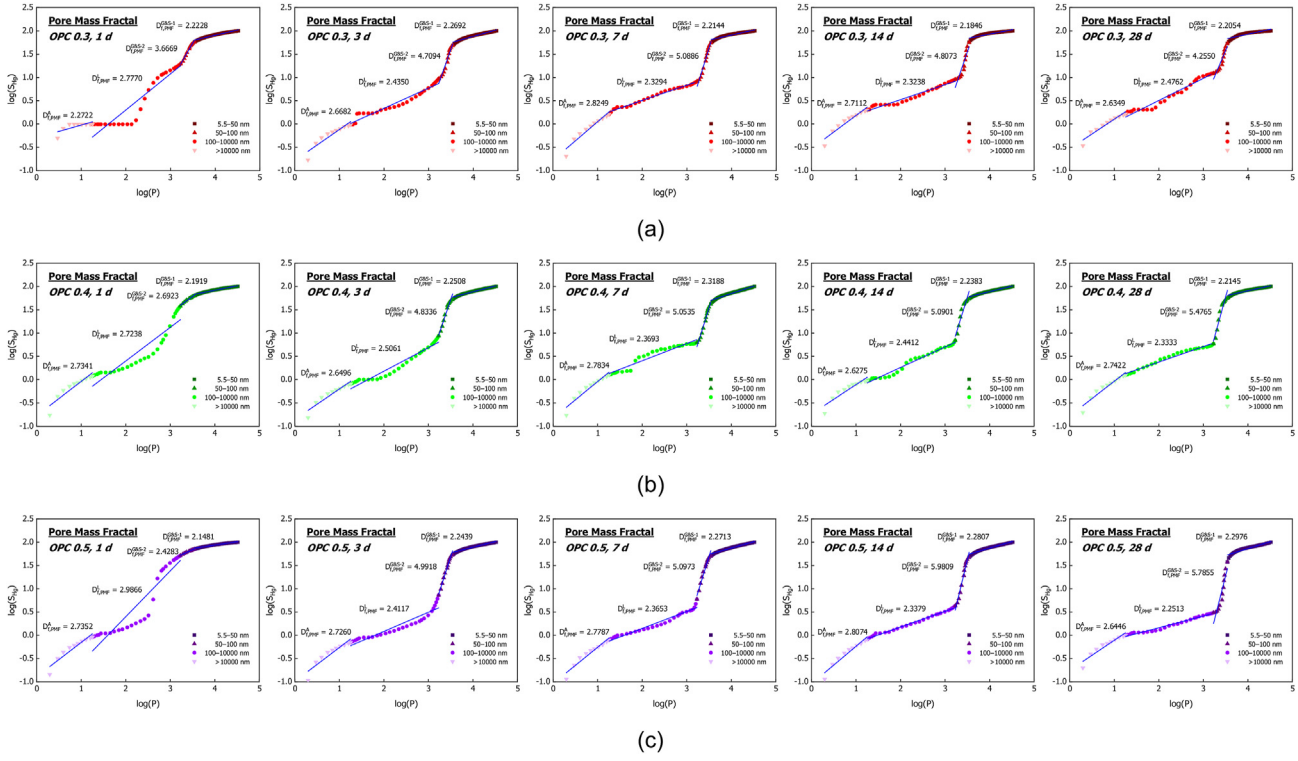

Fig. 4 – Logarithm plots of $\log(P) - \log(S_{Hg})$ for the four pore-size ranges. (a) OPC 0.3; (b) OPC 0.4; and (c) OPC 0.5.

fractal and solid mass fractal, respectively. As shown in Fig. 2(a), $D_{f,PSF}$ for the entire pore-size range was 3.0110. According to the fractal theory, the fractal dimension in space lies between 2 and 3. If the fractal dimension is 2, the structure is perfectly flat (i.e., plane), and if the value is close to 3, it implies that the morphology of the structure has become more complicated [47,48]. Moreover, if the fractal dimension is over 3, the structure is not considered to be physical from the geometric perspective because it deviates from the concept of three-dimensional space [21]. Thus, the result shown in Fig. 2(a) was found to be inconsistent with the fundamental assumption of the fractal theory. Meanwhile, as shown in Fig. 2(b) and (c), $D_{f,PMF}$ and $D_{f,SMF}$ were 2.6798 and 2.9624, respectively, which were within the range of 2–3 mentioned above. However, in the curves of $\log(P) - \log(S_{Hg})$ and $\log(\lambda) - \log(\chi)$, there were clear inflexion points. This suggests that the fractal dimensions derived for the entire pore-size range may present a limitation in precisely representing the entire pore structure characteristics, independent of the applied fractal concepts.

4.1.2. *Various pore-size ranges*

To evaluate in greater detail the variations in the fractal characteristics of the pore structure that is affected by hydration, the pore structure was categorized by the pore-size as follows, according to Monteiro [49] and Mindess et al. [50]: gel & small capillary pores (5.5–50 nm, 50–100 nm), large capillary pores (100–10,000 nm) and air voids (>10,000 nm). Figs. 3–5 show the relationship of $\log(V_{p,n}{}^{1/3}/r_n) - \log(W_n/r_n{}^2)$, $\log(P) - \log(S_{Hg})$ and $\log(\lambda) - \log(\chi)$ for each pore region, respectively. As shown in Figs. 3–5, an inflexion point occurred in common around 50 nm within the region of gel & small capillary pores (particularly, in the concept of mass fractal); thus, the analysis was conducted by dividing the region of gel & small capillary pores into two based on 50 nm to improve the accuracy of fractal analysis. As well known, the fractal dimension has scale-dependency property. Thus, the fractal dimension of local pore region can be derived based on the inflection points present within the entire pore-size range. At this time, the ranges of each local pore region are different for each specimen. The fractal dimension estimated in this way is the actual geometrical characteristic value of the pore structure. However, to analyze the pore structural characteristics within each local pore region that change by hydration, this study focused on the method of classifying the pore region on a constant standard and then analyzing, similar to previous studies [51,52]. In the graphs, the superscripts G&S-1, G&S-2, L and A represent 5.5–50 nm and 50–100 nm of gel & small capillary pores, large capillary pores and air voids, respectively. Table 2 summarizes the estimated $D_{f,PSF}$, $D_{f,PMF}$ and $D_{f,SMF}$ in the four regions.

As shown in Figs. 3–5 and Table 2, $D_{f,SMF}^{G\&S-1}$ and $D_{f,SMF}^{G\&S-2}$ were in the ranges of 2.9156–2.9765 and 2.7428–2.9258, respectively. The fractal dimensions in these pore regions, consisting of the gel pores (corresponding to the pore-size of 5.5–10 nm) and small capillary pores (corresponding to the pore-size of 10–100 nm), tended to increase with increasing age. The $D_{f,SMF}$ reflects the space-filling characteristics of the hydration products for the entire pore structures [18,31], and the increase of this value means that the complexity of the pore structure increases as the fraction of the hydration product increases. The gel pores exist inside the calcium silicate hydrate (C–S–H) gel, which is a component of the C–S–H solid, interlayer space, intra-globule space and monolayer

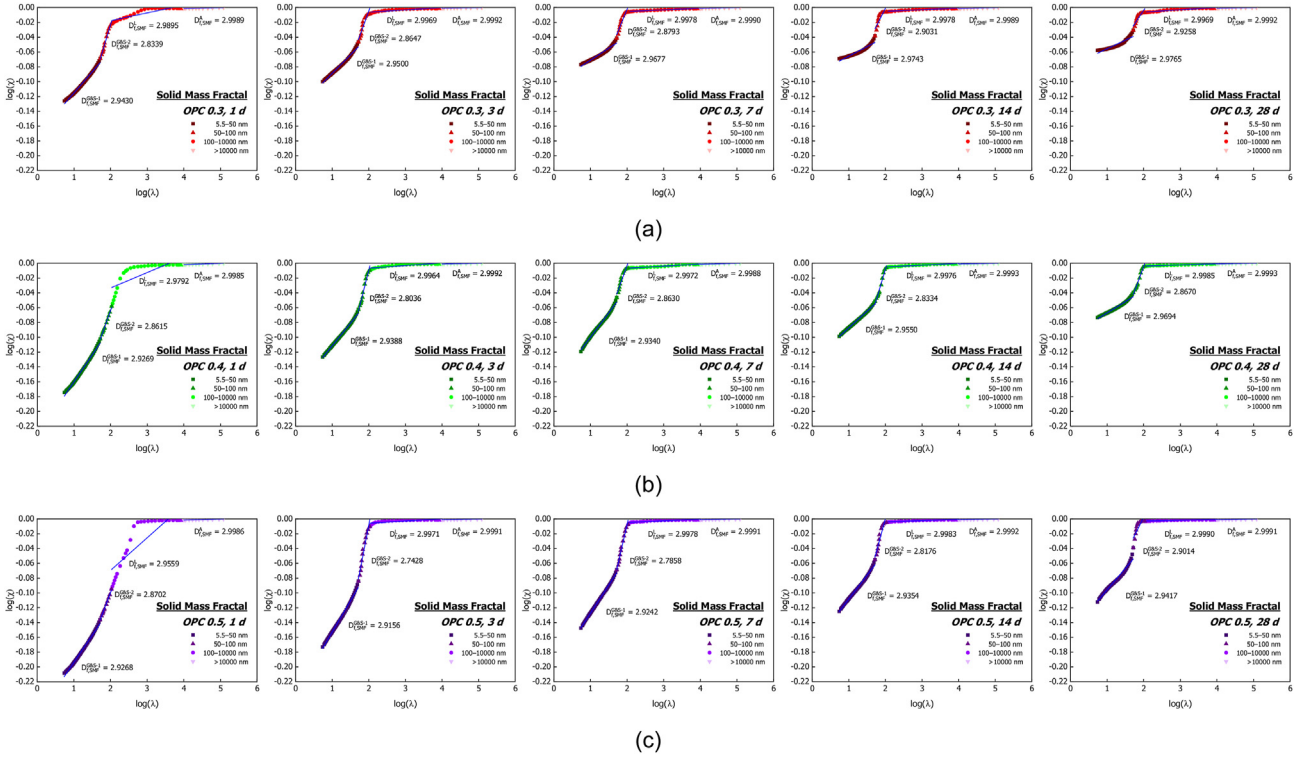

Fig. 5 – Logarithm plots of $\log(\lambda) - \log(\chi)$ for the four pore-size ranges. (a) OPC 0.3; (b) OPC 0.4; and (c) OPC 0.5.

Table 2 – Fractal dimensions on pore-size distribution for the four pore-size ranges.

Specimen	Age (d)	Pore surface fractal dimension				Pore mass fractal dimension				Solid mass fractal dimension			
		Gel & small capillary pores		Large capillary pores	Air voids	Gel & small capillary pores		Large capillary pores	Air voids	Gel & small capillary pores		Large capillary pores	Air voids
		5.5 –50 nm	50 –100 nm	100–10,000 nm	>10,000 nm	5.5 –50 nm	50 –100 nm	100–10,000 nm	>10,000 nm	5.5 –50 nm	50 –100 nm	100–10,000 nm	>10,000 nm
OPC 0.3	1	2.5122	3.3010	3.3492	2.1874	2.2228	3.6669	2.7770	2.2722	2.9430	2.8339	2.9895	2.9989
	3	2.4892	3.4405	3.0379	2.6025	2.2692	4.7094	2.4350	2.6682	2.9500	2.8647	2.9969	2.9992
	7	2.4040	3.7744	2.8906	2.7001	2.2144	5.0886	2.3294	2.8249	2.9677	2.8793	2.9978	2.9990
	14	2.3269	3.8725	3.0115	2.6402	2.1846	4.8073	2.3238	2.7112	2.9743	2.9031	2.9978	2.9989
	28	2.3447	3.8379	3.0540	2.6315	2.2054	4.2550	2.4762	2.6349	2.9765	2.9258	2.9969	2.9992
OPC 0.4	1	2.5371	2.6425	3.1714	2.6262	2.1919	2.6923	2.7238	2.7341	2.9269	2.8615	2.9792	2.9985
	3	2.5076	3.2271	3.1149	2.6174	2.2508	4.8336	2.5061	2.6496	2.9388	2.8036	2.9964	2.9992
	7	2.5535	3.9689	2.8512	2.6692	2.3188	5.0535	2.3693	2.7834	2.9340	2.8630	2.9972	2.9988
	14	2.5046	3.3320	3.0362	2.5731	2.2383	5.0901	2.4412	2.6275	2.9550	2.8334	2.9976	2.9993
	28	2.4342	3.5839	2.8734	2.6671	2.2145	5.4765	2.3333	2.7422	2.9694	2.8670	2.9985	2.9993
OPC 0.5	1	2.5493	2.6313	3.1459	2.6382	2.1481	2.4283	2.9866	2.7352	2.9268	2.8702	2.9559	2.9986
	3	2.4714	3.0982	3.0934	2.6244	2.2439	4.9918	2.4117	2.7260	2.9156	2.7428	2.9971	2.9991
	7	2.5257	3.1598	3.0004	2.6847	2.2713	5.0973	2.3653	2.7787	2.9242	2.7858	2.9978	2.9991
	14	2.4934	3.5420	2.9501	2.6947	2.2807	5.9809	2.3379	2.8074	2.9354	2.8176	2.9983	2.9992
	28	2.4501	3.9772	2.9732	2.6194	2.2976	5.7855	2.2513	2.6446	2.9417	2.9014	2.9990	2.9991

water [53,54]. The C–S–H gel exists in two forms: low density (LD) C–S–H and high density (HD) C–S–H, due to the different packing configurations, of which LD C–S–H tends to be formed in the early hydration stage with sufficient pore spaces inside the cement paste [53,54]. After the initial stage of hydration, as the hydration products are progressively precipitated and accumulated with increasing age, the spaces where the gel pores existed become increasingly complex structurally, leading to the LD C–S–H being converted into HD C–S–H [55]; thus, it was considered that this mechanism affected the increase in both $D_{f,SMF}^{G\&S-1}$ and $D_{f,SMF}^{G\&S-2}$. Small capillary pores are the pores in the range of 10–100 nm as the space between the LD C–S–H and nanoscale hydrated crystals [56]. As the hydration proceeds, an increasing amount of nanoscale hydrated crystals precipitate and grow, contributing to the formation of more complex geometric patterns in the region of small capillary pores.

The $D_{f,PSF}^{G\&S-1}$, $D_{f,PSF}^{G\&S-2}$, $D_{f,PMF}^{G\&S-1}$ and $D_{f,PMF}^{G\&S-2}$ were in the ranges of 2.3269–2.5535, 2.6313–3.9772, 2.1481–2.3188 and 2.4283–5.9809, respectively. While $D_{f,SMF}^{G\&S-1}$ and $D_{f,SMF}^{G\&S-2}$ tended to increase with age, in the case of the concept of pore surface fractal and pore mass fractal, there was no consistent trends in the range of 5.5–50 nm; in addition, in the range of 50–100 nm, it was found that most of the results were over 3, which did not meet the prerequisite of fractal theory. From the results of the region in the range of 5.5–50 nm, it is judged that there is difficulty in analyzing the morphology of the microstructure in terms of the pores since the pore sizes in corresponding region are very fine. In addition, it is inferred that the phenomenon that the fractal dimensions were derived over 3 in the range of 50–100 nm occur due to the following two reasons. One is the existence of ink-bottle pores [57]. Ink-bottle pores have an irregular geometric shape whose inlet diameter is smaller than the inner cavity diameter. Thus, during the MIP measurement, the mercury cannot penetrate the wide inner cavity until sufficient pressure (force required for the mercury to penetrate the narrow inlet) is applied. When sufficient pressure is applied, the quantity of intruded mercury increases sharply to fill the actual inner cavity. Since the pore size corresponding to the narrow inlet is measured as being much larger than the actual one, proper fractal characteristics cannot be obtained. The other reason is the rapid increase of pores in the corresponding region. As hydration progresses, the initial large pores are divided into smaller pores due to the continuous accumulation of hydrates. This can act as a cause of a sharp increase in dimensions in fractal analysis.

In the region of large capillary pores, the, $D_{f,PMF}^{L}$ and $D_{f,SMF}^{L}$ were in the ranges of 2.8512–3.3492, 2.2513–2.9866 and 2.9559–2.9990, respectively. Among the three fractal concepts, only $D_{f,PSF}^{L}$ appeared to be over 3. It seems that a large amount of energy was consumed for mercury injection during the MIP test due to the structural complexity of the large capillary pores region; as a result, the fractal characteristics were not derived in terms of the pore surface. Meanwhile, the parameters $D_{f,PMF}^{L}$ and $D_{f,SMF}^{L}$ tended to decrease and increase, respectively, with increasing age. The parameter $D_{f,PMF}$ represents the geometric characteristics of the pore volume

Table 3 – Univariate analysis results between the degrees of hydration and pore surface fractal dimensions.

Pore surface fractal dimensions												
Parameters	OPC 0.3				OPC 0.4				OPC 0.5			
	Gel & small capillary pores		Large capillary pores	Air voids	Gel & small capillary pores		Large capillary pores	Air voids	Gel & small capillary pores		Large capillary pores	Air voids
	5.5 –50 nm	50 –100 nm	100–10,000 nm	>10,000 nm	5.5 –50 nm	50 –100 nm	100–10,000 nm	>10,000 nm	5.5 –50 nm	50 –100 nm	100–10,000 nm	>10,000 nm
R	−0.92	0.96	−0.77	0.87	−0.67	0.75	0.91	0.18	−0.69	0.96	−0.96	0.24
R^2	0.85	0.92	0.60	0.75	0.45	0.57	0.83	0.03	0.48	0.91	0.92	0.06
p-value	0.03	0.01	0.13	0.06	0.21	0.14	0.03	0.77	0.19	0.01	0.01	0.69

Table 4 – Univariate analysis results between the degrees of hydration and pore mass fractal dimensions.

Pore mass fractal dimensions												
Parameters	OPC 0.3				OPC 0.4				OPC 0.5			
	Gel & small capillary pores		Large capillary pores	Air voids	Gel & small capillary pores		Large capillary pores	Air voids	Gel & small capillary pores		Large capillary pores	Air voids
	5.5 –50 nm	50 –100 nm	100–10,000 nm	>10,000 nm	5.5 –50 nm	50 –100 nm	100–10,000 nm	>10,000 nm	5.5 –50 nm	50 –100 nm	100–10,000 nm	>10,000 nm
R	−0.50	0.59	−0.79	0.78	0.28	0.95	−0.95	−0.07	0.96	0.93	−0.91	−0.14
R^2	0.25	0.35	0.62	0.60	0.08	0.90	0.90	0.00	0.92	0.86	0.82	0.02
p-value	0.39	0.30	0.12	0.12	0.64	0.01	0.01	0.92	0.01	0.02	0.03	0.83

distribution. As the hydration proceeds, the volume fractions corresponding to the large capillary pores decreased; thus, structural complexity in that region appeared to decrease in the pore mass aspects. Conversely, $D_{f,SMF}$ reflects the space-filling characteristics of the hydration products. As the hydration proceeds, the decrease in volume fractions corresponding to the large capillary pores indicates that the solid volume fractions in that region increase. Thus, the structural complexity increased in the solid mass aspects, as the hydration products contribute to transform the loose initial structure into a dense one through the interconnection and space-filling of the pore structure [58].

Lastly, the parameters $D^{A}_{f,PSF}$, $D^{A}_{f,PMF}$ and $D^{A}_{f,SMF}$ were in the range of 2.1874–2.7001, 2.2722–2.8249 and 2.9985–2.9993, respectively. The air voids correspond to a very large pore region of more than 10,000 nm. When the concepts of the pore surface fractal and pore mass fractal were used, distinct variation trends were not observed with increasing age compared to the other regions. By contrast, $D^{A}_{f,SMF}$ tended to increase with increasing age, however, the sensitivity of the results was insufficient. This leads to a limitation in that a clear distinction between different fractal characteristics from specimen to specimen is difficult.

As summarizing the results of Table 2, it was confirmed that the solid mass fractal dimensions in all pore regions and the pore mass fractal dimensions in the region of large capillary pores varied with a consistent tendency according to the variation of ages. That is to say, this indicates that the age-related properties of the specimens can be estimated through the variation tendency of fractal dimensions. Furthermore, the morphology of the microstructure at a specific age can be presumed by comparison with the fractal dimension of an ideal fractal structure [59].

4.1.3. *Correlation among the three different concepts of fractal dimensions of pore-size distribution and hydration*

As mentioned above, since the three concepts of fractal dimensions of pore-size distribution are derived from different aspects (pore surface, pore mass and solid mass), the suitable parameters may vary depending on the target materials. Since the pore structure of the cementitious material changes as the hydration proceeds, it is necessary to determine the representative fractal concept that is the most suitable for analyzing the geometric characteristics of the pore structure of the cementitious material in consideration of the hydration. Tables 3–5 show the univariate analysis results of the relationship between the degrees of hydration and fractal dimensions derived from the three fractal concepts. Since the correlation and causality between these two parameters can be quantitatively evaluated by the Pearson correlation coefficient (R) and the coefficient of determination (R^2), this study conducted the analysis using such two coefficients. The degree of hydration of the cement paste was obtained from Power's model [60], as follows:

$$\alpha = \frac{(1-\varphi^{c})(W/C) - 0.32\varphi^{c}}{0.36} \tag{12}$$

where α denotes the degree of hydration, W/C denotes the water-to-cement ratio, and φ^{c} denotes the capillary porosity.

Table 5 – Univariate analysis results between the degrees of hydration and solid mass fractal dimensions.

Solid mass fractal dimensions	OPC 0.3				OPC 0.4				OPC 0.5			
Parameters	Gel & small capillary pores		Large capillary pores	Air voids	Gel & small capillary pores		Large capillary pores	Air voids	Gel & small capillary pores		Large capillary pores	Air voids
	5.5 –50 nm	50 –100 nm	100–10,000 nm	>10,000 nm	5.5 –50 nm	50 –100 nm	100–10,000 nm	>10,000 nm	5.5 –50 nm	50 –100 nm	100–10,000 nm	>10,000 nm
R	0.97	0.97	0.85	0.35	0.88	0.05	0.91	0.83	0.66	0.17	0.84	0.84
R^2	0.94	0.94	0.73	0.12	0.77	0.00	0.83	0.69	0.44	0.03	0.70	0.70
p-value	0.01	0.01	0.07	0.57	0.05	0.93	0.03	0.08	0.34	0.83	0.08	0.08

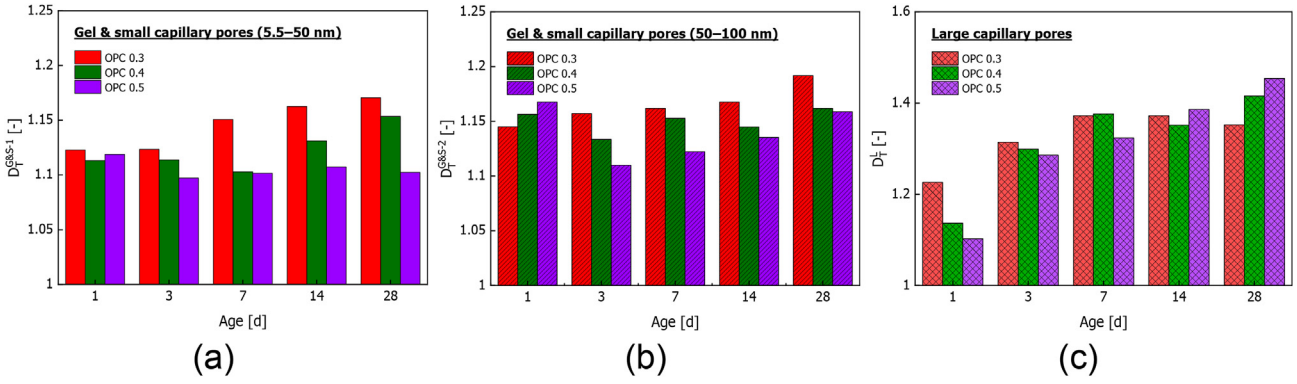

Fig. 6 – Variations of fractal dimensions of pore tortuousness depending on the age. (a) gel & small capillary pores (5.5–50 nm); (b) gel & small capillary pores (50–100 nm); and (c) large capillary pores.

For the correlation and regression analysis, the data of degrees of hydration and fractal dimensions were imported into Excel. The scatter plot between the degrees of hydration and the fractal dimensions was drawn by Excel; and then, R^2 and R were obtained by linear regression analysis and correlation analysis, respectively. In addition, the t-test was used to reveal the significance of the correlation.

In Tables 3–5, R can quantifies how well the degrees of hydration and fractal dimensions of pore-size distribution are correlated to each other and evaluates the variation tendency between such two parameters. Generally, as the hydration proceeds (i.e., the degree of hydration increases), the hydration products become increasingly precipitate and grow in the pore spaces. Therefore, the large pores tend to be divided into small pores, and the pore structure becomes dense. In the region of the gel & small capillary pores, both the pore volume fraction and solid volume fraction increase together. Thus, the fractal dimensions of pore-size distribution derived from both the pore mass and solid mass concepts showed positive correlations with the degrees of hydration. By contrast, in the region of the large capillary pores, the opposite correlation tended to be observed according to the fractal concept (negative correlation in the pore mass fractal concept and positive correlation in the solid mass fractal concept). As the hydration proceeds, the pore volume fractions in the region of the large capillary pores gradually decrease, but the hydration products are formed continuously. The geometric characteristics in the concept of the pore mass fractal originate from the pore space; thus, the fractal dimensions tended to decrease with increasing degrees of hydration. However, the geometric characteristics in the solid mass fractal concept originate from the solid space (i.e., hydration products space); thus, the fractal dimensions tended to increase with increasing degrees of hydration. Meanwhile, as a result of analyzing the geometric characteristics of the pore surface, results similar to those of the pore mass were found in the regions of gel & small capillary pores (50–100 nm) and large capillary pores. However, in the region of gel & small capillary pores (5.5–50 nm), the complexity of the surface decreased as the hydration progressed. This is considered to be because, as hydrates are generated, the pores corresponding to the range of 50–100 nm are rapidly increased and the surface thereof become complicate, however, the topography in the finer pore region is rather arranged regularly, leading to reduce the complexity thereof.

As summarizing the results of R, although a very low quantitative coefficients were derived from about one-third of the results for each concept, other results showed that a "strong" relation between the two parameters, and that as the degree of hydration changed by hydration reactions, this change causes the change in fractal dimension. Additionally, for the solid mass fractal concept, unlike the other two concepts, consistent trend appeared with the degree of hydration in all pore regions regardless of the w/c.

As shown in Tables 3–5, R^2 between the degrees of hydration and $D_{f,PSF}$, $D_{f,PMF}$ and $D_{f,SMF}$ were in the ranges of 0.03–0.92, 0.00–0.92 and 0.00–0.94, respectively. R^2 can evaluates the extent to which changes in hydration affect the changes in fractal dimensions. With an exception of few cases where the causality were remarkably degraded, the degrees of hydration appeared to have a significant relationship with the three concepts of fractal dimensions, and the best correlation was observed probabilistically between the degrees of hydration and the solid mass fractal dimensions. In addition, the p-value (significance probability) derived from the t-test appeared to be lower than 0.1 (correlation is significant at the 0.1 level, p-value < 0.1, 2-tailed) (except for the few cases mentioned above). This was probabilistically lower than the p-value derived between the degrees of hydration and the other two concepts of fractal models.

Such results indicate that the fractal dimension can sufficiently represent the characteristics of microstructures that change with hydration. As summarizing the results of section 4.1.2 and 4.1.3, in the case of applying the solid mass fractal concept, the derived results were not deviate from its physical meaning in all pore regions, and the tendency of change in the geometric characteristics of the pore structure was analyzed apparently. In addition, it had the most significant relationship with the hydration of cement pastes. Therefore, we deduced that the solid mass fractal concept is a representative concept that can effectively describe the geometric characteristics of the pore structure of cementitious material.

Table 6 – Pearson correlation coefficient *R* derived through the univariate analysis results among the pore structure characterization parameters.

	λ_{th}	λ_{cr}	φ^{T}	$\varphi^{G\&S-1}$	$\varphi^{G\&S-2}$	φ^{L}	$\varepsilon^{G\&S-1}$	$\varepsilon^{G\&S-2}$	ε^{L}	$D_f^{G\&S-1}$	$D_f^{G\&S-2}$	D_f^{L}	$D_T^{G\&S-1}$	$D_T^{G\&S-2}$	D_T^{L}
λ_{th}	1.00	–	–	–	–	–	–	–	–	–	–	–	–	–	–
λ_{cr}	0.99	1.00	–	–	–	–	–	–	–	–	–	–	–	–	–
φ^{T}	0.70*	0.62	1.00	–	–	–	–	–	–	–	–	–	–	–	–
$\varphi^{G\&S-1}$	0.12	0.06	0.74*	1.00	–	–	–	–	–	–	–	–	–	–	–
$\varphi^{G\&S-2}$	−0.14	−0.21	0.51	0.70*	1.00	–	–	–	–	–	–	–	–	–	–
φ^{L}	0.97*	0.94*	0.71*	0.11	−0.17	1.00	–	–	–	–	–	–	–	–	–
$\varepsilon^{G\&S-1}$	−0.72*	−0.69*	−0.32	0.38	0.16	−0.75*	1.00	–	–	–	–	–	–	–	–
$\varepsilon^{G\&S-2}$	−0.80*	−0.77*	−0.67*	−0.33	0.27	−0.86*	0.34	1.00	–	–	–	–	–	–	–
ε^{L}	0.68*	0.58	0.52	−0.01	−0.20	0.83*	−0.72*	−0.73*	1.00	–	–	–	–	–	–
$D_f^{G\&S-1}$	−0.41	−0.33	−0.93*	−0.93*	−0.70*	−0.41	−0.01	0.49	−0.28	1.00	–	–	–	–	–
$D_f^{G\&S-2}$	0.03	0.10	−0.56	−0.64	−0.98*	−0.07	−0.02	−0.22	0.11	0.70*	1.00	–	–	–	–
D_f^{L}	−0.98*	−0.97*	−0.67*	−0.07	0.21	−0.99*	0.74*	0.84*	−0.76*	0.37	−0.10	1.00	–	–	–
$D_T^{G\&S-1}$	−0.17	−0.11	−0.77*	−0.99*	−0.69*	−0.16	−0.33	0.36	−0.04	0.93*	0.65*	0.12	1.00	–	–
$D_T^{G\&S-2}$	0.15	0.22	−0.51	−0.73*	−0.98*	0.18	−0.21	−0.25	0.21	0.70*	0.96*	−0.22	0.73*	1.00	–
D_T^{L}	−0.81*	−0.73*	−0.74*	−0.16	−0.07	−0.89*	0.78*	0.71*	−0.88*	0.50	0.19	0.86*	0.22	0.05	1.00

* Represents that the results of the correlation analysis at the significant level of 0.01 is remarkable.
Here, λ, φ, and ε denote pore diameter, porosity and pore volume fraction, respectively.

4.2. *Fractal dimension of pore tortuousness*

Fig. 6 shows the variations of fractal dimensions of pore tortuousness depending on the age in the region of the gel & small capillary pores (5.5–50 nm and 50–100 nm) and the large capillary pores. In the graphs, the subscript T represents the tortuousness. The D_T for each pore region was calculated by Eq. (10) using the average tortuosity, obtained by Eq. (11) through the porosity of each pore region derived by the MIP test, L_0, estimated in this study, and the average pore diameter of each pore region. As shown in Fig. 6, $D_T^{G\&S-1}$, $D_T^{G\&S-2}$ and D_T^{L} were in the ranges of 1.0972–1.1706, 1.1098–1.1918 and 1.1024–1.4536, respectively. In the specimens with the same w/c and pore region, the fractal dimensions of pore tortuousness tended to increase with increasing age. This tendency was noticeable in the region of gel & small capillary pores for the specimen with a low w/c, and was noticeable in the region of large capillary pores for the specimen with a high w/c. From this result, it was found that, as the hydration of cement particles develops, the pore paths inside the pore structure become more tortuous. Moreover, the effect of the conditions of the initial pore space according to the w/c on the morphology of pore paths was different for each pore region.

As shown in Fig. 6(a) and (b), $D_T^{G\&S-1}$ and $D_T^{G\&S-2}$ increased with decreasing w/c (except for one day). Since the amount of water decreases with decreasing w/c under the same amount of cement, the less initial pore space is formed in the specimen with a low w/c compared to that with a high w/c. Thus, due to the high probability that the hydration products grow while overlapping each other in a confined pore space, the high tortuosity of the pore paths was observed in the specimen having a low w/c with the less initial pore space. Meanwhile, as shown in Fig. 6(c), D_T^{L} tended to increase with decreasing w/c at the early ages (one and 3 days). Conversely, D_T^{L} tended to decrease with decreasing w/c at the later age of 28 days. As mentioned above, because the hydration products are filled in an initial confined pore space in the specimen with a low w/c, the tortuousness of the large capillary pores increases. However, as the w/c increases, the reaction occurs actively and continuously, resulting in a steady growth of the hydration products in the microstructure compared to the specimen with a low w/c. Therefore, we considered that the variation trend of D_T^{L} was reversed. This phenomenon was also confirmed by the results, where the increase in the ratios of D_T^{L} at 28 days to that of one day increased to 10.29%, 24.51% and 31.86% for OPC 0.3, OPC 0.4 and OPC 0.5, respectively.

As such, D_T^{L} increased with increasing w/c at the later ages, whereas $D_T^{G\&S-1}$ and $D_T^{G\&S-2}$ tended to decrease with increasing w/c. Although the specimen having a high w/c showed high tortuousness for the large capillary pores because the hydration products grow continuously in that region, there is less tendency for hydration products to grow overlapping each other due to the large initial pore space. Consequently, we reasoned that the reversal of the variation trend of the fractal dimensions of pore

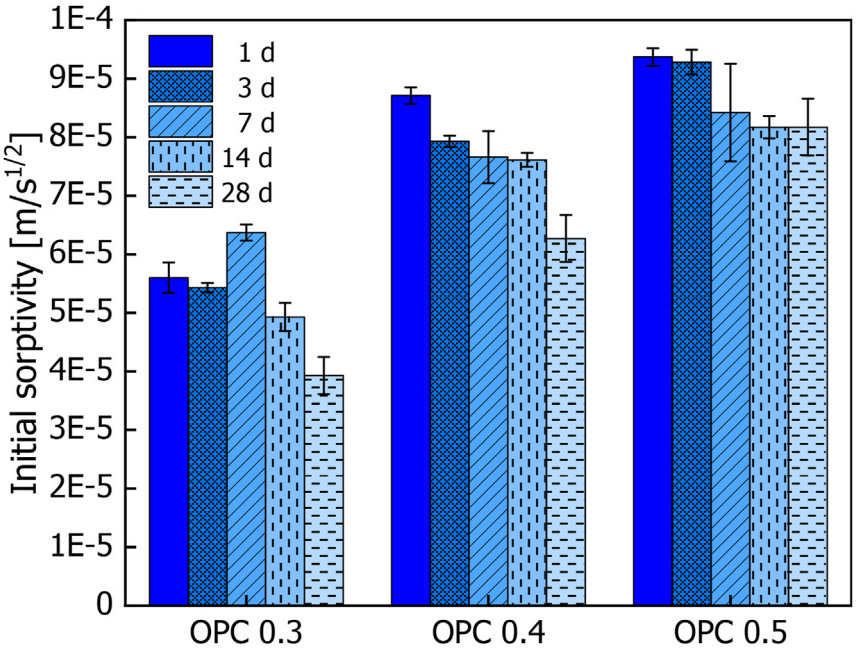

Fig. 7 – Initial sorptivity of the specimens.

tortuousness depending on the w/c, which resulted from the difference in hydration rate, does not affect the two regions of the gel & small capillary pores (5.5–50 nm and 50–100 nm) in the specimen having a high w/c.

As summarizing all the results, the conditions of the initial pore space and the degree of hydration according to the w/c affect the formation of microstructure, which lead to the variation of D_T; thus, we judged that it is possible to characterize the pore structure with the parameter of D_T.

4.3. *Correlation among the pore structure characterization parameters*

Table 6 shows R derived through the univariate analysis results among the pore structure characterization parameters. In the table, the subscripts th and cr represent the threshold and critical pore diameter, respectively, and the superscript T represents the total pore region. As shown in Table 6, the R of $D_f - \varphi$ (the relationship between D_f and φ corresponding to each pore region) and $D_T - \varphi$ (the relationship between D_T and φ corresponding to each pore region) lies in the ranges of 0.93–0.99 and 0.75–0.99, respectively (negative correlation). Given that the correlation between the two parameters is interpreted as strong and very strong when R lies in the ranges of 0.70–0.89 and 0.90–1.00, respectively [61], D_f and D_T for each pore region appeared to have strong and very strong negative correlations with the porosity for each corresponding region. The porosity is one of the representative parameters that can characterize the pore structure. Such the high correlations between the porosity and geometric pore structure characterization parameters indicate that the pore structure can be sufficiently characterized by the geometric parameters of D_f and D_T, as well as the existing volumetric ones (porosity) [62]. Furthermore, since D_f and D_T react more sensitively to changes in the pore structure, it was considered that the pore structure can be characterized more precisely than the case where only the existing volumetric pore structure characterization parameters were utilized [62,63].

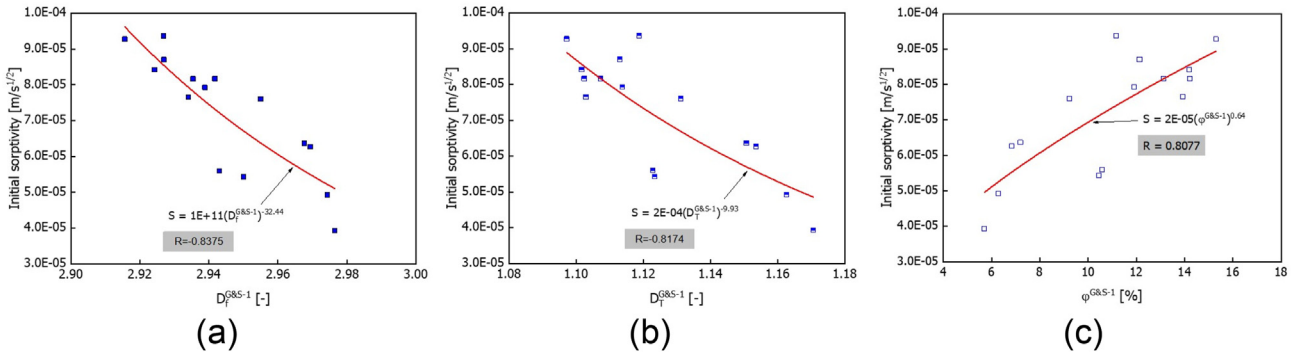

Fig. 8 – Relationship between the pore structure characterization parameters and initial sorptivity. (a) with $D_f^{G\&S-1}$; (b) with $D_T^{G\&S-1}$; (c) with $\varphi^{G\&S-1}$.

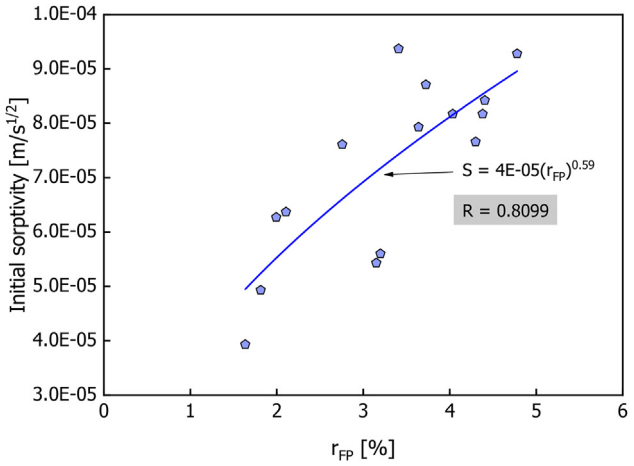

Fig. 9 – Relationship between r_{FP} and initial sorptivity.

Meanwhile, R between the pore volume fraction ε of the gel & small capillary pores (5.5–50 nm and 50–100 nm) and the large capillary pores showed negative correlations. This result indicates that the pore structure becomes dense due to the microstructure filling effect of the hydration products. In addition, the ε in these regions showed strong correlations with φ^{L}, D_f^{L}, D_T^{L} and λ_{th}. From these results, it was inferred that the densification of the pore structure has a significant influence on both the volumetric and geometric characteristics of the large capillary pores among the three pore regions.

4.4. *Analysis of the water sorption ability of cement paste*

4.4.1. *Water absorption test results*

The results of the initial sorptivity of the specimens are shown in Fig. 7. At the same w/c, the initial sorptivity tended to decrease with increasing age (except for OPC 0.3 specimen at 7 days). As the age increases, hydration products increasingly fill the pore structure, making it denser; thus, the ability of water uptake through the interconnected pore paths seems to decrease. In addition, at the same age, the initial sorptivity decreased with decreasing w/c. As described above, the specimens with a low w/c have the less initial pore space; hence, it may affect the decrease in the initial sorptivity.

4.4.2. *Correlation among porosity, fractal dimensions and initial sorptivity*

To verify the effectiveness of applying fractal geometry on interpreting the transport properties of cementitious materials, first, the initial sorptivity relative to $D_f^{G\&S-1}$, $D_T^{G\&S-1}$ and $\varphi^{G\&S-1}$ were investigated separately (among the four pore regions, the volumetric and geometric pore structure characterization parameters in the 5.5–50 nm of gel & small capillary pores showed the best correlation with initial sorptivity). The initial sorptivity plotted against $D_f^{G\&S-1}$ and $D_T^{G\&S-1}$ are shown in Fig. 8(a) and (b), respectively. The $D_f^{G\&S-1}$–S (the relationship between $D_f^{G\&S-1}$ and S) and $D_T^{G\&S-1}$–S (the relationship between $D_T^{G\&S-1}$ and S) appeared to be a power function with strong correlations (−0.8375 and −0.8174 of R, respectively). In addition, the exponents in the regression equations were negative numbers, which indicate that higher $D_f^{G\&S-1}$ and $D_T^{G\&S-1}$ lead to lower initial sorptivity. As described earlier, the increased fractal dimensions indicate that the complexity of the pore structure increases in terms of both the pore-size distribution and pore tortuousness; thus, it seems to affect the decrease in initial sorptivity. The initial sorptivity plotted against $\varphi^{G\&S-1}$ is shown in Fig. 8(c). The $\varphi^{G\&S-1}$–S (the relationship between $\varphi^{G\&S-1}$ and S) also appeared to be a power function with a strong correlation (0.8077 of R). However, unlike Fig. 8(a) and (b), the regression exponent was a positive number, which indicates that higher porosity leads to higher initial sorptivity.

Porosity is the most well-known physical quantity that is measured directly through the MIP test, and that is the primary characteristic that significantly affects the transport ability of cementitious materials [64]. However, even if the pore structures of cementitious materials have the similar porosity, different transport properties may be observed depending on their structural shape. Thus, if the fractal dimensions are additionally used for the analysis of the transport properties, the existing results, which were difficult to analyze, may be newly interpreted. Fig. 9 shows the relationship between the initial sorptivity and the newly derived parameter considering both the volumetric and geometric ones. As shown in Fig. 8, since the two types of fractal dimensions and the porosity were simultaneously related to the initial sorptivity as the negative and positive power function, respectively, r_{FP} can be derived in terms of $D_f^{G\&S-1}$, $D_T^{G\&S-1}$ and $\varphi^{G\&S-1}$, as follows:

$$r_{FP} = \frac{\varphi^{G\&S-1}}{D_f^{G\&S-1} \cdot D_T^{G\&S-1}} \tag{13}$$

Thus, through the regression analysis shown in Fig. 9, the initial sorptivity can be expressed simply by using the following equation:

$$S = 4E-05 \cdot (r_{FP})^{0.59} \tag{14}$$

Among the experimental conditions of the water absorption test applied in this study, the boundary condition of the specimen and submerged water level affect the initial sorptivity. If the side and top surfaces of the specimen are not sealed, the water absorbed into the capillaries will evaporate during the experiment, causing a decrease in initial sorptivity. In addition, the capillary pressure leading to the initial water absorption is mainly affected by the diameter of capillaries. However, if the submerged water level is different, the pressure acting on the specimen vary, also leading to affect the initial sorptivity. Therefore, the regression result of Eq. (14) is valid for specimens with the same experimental conditions as in this study. As shown in Fig. 9, the correlation coefficient also indicates a strong correlation, which is $R = 0.8099$, and the simply derived theoretical curve was consistent with the experimental results. Compared to the existing analytic methods, the transport ability of cement pastes can also be interpreted pretty accurately using both the volumetric and geometric parameters. Moreover, the fractal dimension acts as a much more accurate quantitative parameter to

characterize the pore structure than that already used [63]. In addition, as mentioned above, the reason why the specimens with similar porosity show different transport properties can be analyzed further. Putting it concisely, it is expected that the interpretation of the transport properties of cementitious materials from various perspectives will be possible via the simultaneously use of parameters from different aspects that can describe the pore structure.

5. Further research

In the field of studying on the pore structures of porous materials, applying fractal geometry is quite a novel research technique, and the results derived from it are being used meaningfully in various research fields. Although significant results were derived from this study, several aspects should be studied further.

The present results of this study are for the pore structure measured via the MIP test. Since the pore structures can be analyzed through various experimental techniques, the reproducibility of the results may limit when other experimental techniques are used. By comparing the results derived using various experimental techniques, the currently conducted fractal utilization analysis technique can be further developed.

Oven drying at 105 °C, which is the pretreatment method of the MIP test, is one of the effective techniques to remove evaporable water. However, it is also the method of changing the microstructure of the hardened cement paste as decomposition of hydration products may occur during the drying process [65]. For instance, the dehydrate of gypsum, ettringite and C–S–H is known to occur approximately 60–105 °C [36,66–68]. Accordingly, it is judged that additional research on the drying method to prevent the destructive effect on the microstructure is needed.

This study conducted the correlation and regression analysis on the specimens with different degree of hydration. However, there is a limit to generalizing the analysis results in that the number of specimens and type of mixtures are limited. Therefore, further analysis is necessary by building up the related database through the additional experiments, that can measure the degree of hydration, and the use of various cementitious materials.

In this study, the efficiency of using the fractal dimensions was demonstrated by analyzing the correlation between the parameter, using both the volumetric and geometric ones, and the initial sorptivity of cementitious material. Meanwhile, as mentioned above, even in the pore structures with similar volumetric characteristics, the development of engineering properties may vary depending on different geometric ones. However, there were limitations in that it was difficult to derive reliable results since there were insufficient cases of microstructure analyzed in this study. In further research, it is expected that meaningful results can be derived in the field of microstructure analysis using fractal theory through the design and implementation of more specific experimental cases to prove this.

In addition to the MIP test used in this study, various techniques that can evaluate the pore structure of cementitious materials exist, and one of which is the image analysis. Fu and Yu [69] conducted a research on the analysis of various characteristics of pore structure through image processing techniques and MATLAB programs using the images of pore structure of concrete taken by X-ray computed tomography (CT). Using X-ray CT, the image can be obtained without damaging the pore structure [69]. Since the analysis is conducted based on the images, the information on the pore structure that is difficult to measure by the MIP test, such as the connectivity between pores, can be obtained [70]. Accordingly, it is necessary to conduct a research on developing the existing technique by applying fractal theory to the image analysis technique on the pore structure of cementitious materials, and analyzing the difference by comparing such results with the results of this study, in-depth.

Wood [71] conducted a research on techniques for calculating fractal dimension of organic-rich shale considering the uncertainties and discrepancies that may occur when deriving fractal dimension. The fractal dimension of organic-rich shale is typically derived by applying Frenkel-Halsey-Hill (FHH) technique to the isotherm curve obtained through the gas adsorption experiment. However, the problem is that using FHH technique alone cannot solve the uncertainties. Therefore, in Wood's research [71], in addition to the FHH technique, Neimark (NM) [41] and Wang and Li (WL) [72] techniques were used to analysis the discrepancies and uncertainties related to the derived fractal dimensions. Additionally, the fitting process utilized in each technique was evaluated, and methods for optimizing and standardizing the analysis were studied. Cementitious materials also have a very complex microstructure similar to shale and, in this study, although the fractal dimensions were derived using models derived from three fractal concepts, uncertainties on the results were existed similar to Wood's research [71]. Thus, it is necessary to develop an analysis technique that can integrate the fractal concepts that affects the fractal properties of the microstructure of cementitious materials while resolving such uncertainties.

6. Summary and conclusions

In this study, the development of the pore structure of hydrated cement paste was analyzed via experimental and fractal approaches. In addition, the ability of applying fractal geometry on interpreting the transport properties of hydrated cement pastes from various perspectives was evaluated via sorptivity. The main conclusions are summarized as follows:

1) The fractal dimension of pore-size distribution can be quantified in terms of the pore surface, pore mass and solid mass aspects. As a result of the correlation analysis between the fractal dimensions and the degrees of hydration, it was found that the fractal dimensions of pore-size distribution can be investigated most suitably in interpreting the characteristics of pore structure when derived from the solid mass aspect. As the solid fraction within the entire microstructure increased due to the filling effect of hydration products, the morphological complexity of the pore-size distribution tended to increase in all the pore regions.

2) In terms of the fractal characteristics of pore tortuousness, the complexity in the region of the gel & small capillary pores increased with decreasing w/c. It was considered that this result was due to the growth of the hydration products overlapping each other because of the narrow pore space in the specimen having a low w/c. This phenomenon was also observed in the region of the large capillary pores at the early ages. However, as the age progressed, the tendency was reversed due to the rapid hydration of the specimen having a high w/c.
3) The analysis of the correlation between the geometric pore structure characterization parameters and the existing ones revealed that the fractal dimensions to be highly correlated with the volumetric characteristics. This indicates that D_f and D_T can be sufficiently utilized as parameters to characterize the pore structure.
4) The porosity and the two types of fractal dimensions showed positive and negative power function relation with initial sorptivity, respectively. Accordingly, the ratio of porosity to the multiplication of D_f and D_T was newly derived for analyzing the relationship between the microstructural characterizations and the initial sorptivity. The findings from the regression analysis showed that the utilization of both the volumetric and geometric parameters acts complementary in interpreting the transport properties of cementitious materials from various perspectives.

CRediT authorship contribution statement

Jiyoung Kim: Conceptualization, Methodology, Validation, Formal analysis, Investigation, Resources, Data curation, Writing – original draft, Writing – review & editing, Visualization. **Geuntae Hong:** Methodology, Investigation, Data curation. **Sangwoo Oh:** Validation, Formal analysis, Investigation, Data curation. **Seongcheol Choi:** Conceptualization, Validation, Investigation, Resources, Writing – review & editing, Supervision, Project administration, Funding acquisition.

Declaration of Competing Interest

The authors declare that they have no known competing financial interests or personal relationships that could have appeared to influence the work reported in this paper.

Acknowledgements

This work was supported by the Korea Agency for Infrastructure Technology Advancement (KAIA) grant funded by the Ministry of Land, Infrastructure and Transport (Grant 22SCIP-C159049-03). This work was also supported by the National Research Foundation of Korea (NRF) grant funded by the Korea government (MSIT) (No. 2021R1F1A1062654).

REFERENCES

[1] Chen X, Wu S, Zhou J. Influence of porosity on compressive and tensile strength of cement mortar. Construct Build Mater 2013;40:869–74.
[2] Cui L, Cahyadi JH. Permeability and pore structure of OPC paste. Cement Concr Res 2001;31(2):277–82.
[3] Sakai Y. Relationship between pore structure and chloride diffusion in cementitious materials. Construct Build Mater 2019;229:116868.
[4] Li Y, Bao J, Guo Y. The relationship between autogenous shrinkage and pore structure of cement paste with mineral admixtures. Construct Build Mater 2010;24(10):1855–60.
[5] Netinger Grubeša I, Marković B, Vračević M, Tunkiewicz M, Szenti I, Kukovecz Á. Pore structure as a response to the freeze/thaw resistance of mortars. Materials 2019;12(19):3196.
[6] Zhang J, Bian F, Zhang Y, Fang Z, Fu C, Guo J. Effect of pore structures on gas permeability and chloride diffusivity of concrete. Construct Build Mater 2018;163:402–13.
[7] Sanchez F, Ince C. Microstructure and macroscopic properties of hybrid carbon nanofiber/silica fume cement composites. Compos Sci Technol 2009;69(7–8):1310–8.
[8] Choi YC, Kim J, Choi S. Mercury intrusion porosimetry characterization of micropore structures of high-strength cement pastes incorporating high volume ground granulated blast-furnace slag. Construct Build Mater 2017;137:96–103.
[9] Van Breugel K. Simulation of hydration and formation of structure in hardening cement-based materials [Ph.D. thesis]. Delft: Delft University of Technology; 1991.
[10] Bentz DP, Garboczi EJ. Digitised simulation model for microstructural development. Ceram Trans 1990;16:211–26.
[11] Ozturk AU, Baradan B. A comparison study of porosity and compressive strength mathematical models with image analysis. Comput Mater Sci 2008;43(4):974–9.
[12] Chen X, Zhou J, Ding N. Fractal characterization of pore system evolution in cementitious materials. KSCE J Civ Eng 2015;19(3):719–24.
[13] Olson RA, Neubauer CM, Jennings HM. Damage to the pore structure of hardened Portland cement paste by mercury intrusion. J Am Ceram Soc 1997;80(9):2454–8.
[14] Mahamud M, López Ó, Pis JJ, Pajares JA. Textural characterization of coals using fractal analysis. Fuel Process Technol 2003;81(2):127–42.
[15] Niu D, Li D, Fu Q. A 3D-IFU model for characterizing the pore structure of hybrid fibre-reinforced concrete. Mater Des 2020;188:108473.
[16] Mandelbrot BB. Fractals: form, chance and dimension, Fractals: form, chance and dimension. San Francisco (CA, USA): WH Freeman & Co.; 1979.
[17] Cai J, Zhang L, Ju Y, Pia G, Zhang Z. An introduction to fractal-based approaches in unconventional reservoirs—part I. Fractals 2018;26(2):1802001.
[18] Kim J, Choi S. A fractal-based approach for reconstructing pore structures of GGBFS-blended cement pastes. Construct Build Mater 2020;265:120350.
[19] Taylor HF. Cement chemistry, vol. 2. London: Thomas Telford; 1997.
[20] Ji X, Chan SYN, Feng N. Fractal model for simulating the space-filling process of cement hydrates and fractal dimensions of pore structure of cement-based materials. Cement Concr Res 1997;27(11):1691–9.
[21] Zhang B, Li S. Determination of the surface fractal dimension for porous media by mercury porosimetry. Ind Eng Chem Res 1995;34(4):1383–6.

[22] Lange DA, Jennings HM, Shah SP. Image analysis techniques for characterization of pore structure of cement-based materials. Cement Concr Res 1994;24(5):841–53.
[23] Wang Y, Diamond S. A fractal study of the fracture surfaces of cement pastes and mortars using a stereoscopic SEM method. Cement Concr Res 2001;31(10):1385–92.
[24] Winslow DN. The fractal nature of the surface of cement paste. Cement Concr Res 1985;15(5):817–24.
[25] Kim J, Choi YC, Choi S. Fractal characteristics of pore structure in GGBFS-based cement pastes. Appl Surf Sci 2018;428:304–14.
[26] Yang J, Wang F, He X, Su Y. Pore structure of affected zone around saturated and large superabsorbent polymers in cement paste. Cem Concr Compos 2019;97:54–67.
[27] Yang J, Su Y, He X, Tan H, Jiang Y, Zeng L, et al. Pore structure evaluation of cementing composites blended with coal by-products: calcined coal gangue and coal fly ash. Fuel Process Technol 2018;181:75–90.
[28] Bednarska D, Wieczorek A, Koniorczyk M. Characterization of pore structure for permeability prediction of cement based materials under frost attack-The fractal approach. In: AIP conference proceedings. Vol. 2018. AIP Publishing LLC; 1988, 020005.
[29] Friesen WI, Mikula RJ. Fractal dimensions of coal particles. J Colloid Interface Sci 1987;120(1):263–71.
[30] Li K. Analytical derivation of Brooks–Corey type capillary pressure models using fractal geometry and evaluation of rock heterogeneity. J Pet Sci Eng 2010;73(1–2):20–6.
[31] Usteri M, Bonny JD, Leuenberger H. Fractal dimension of porous solid dosage forms. Pharm Acta Helv 1990;65(2):55–61.
[32] Xu P, Yu B. Developing a new form of permeability and Kozeny-Carman constant for homogeneous porous media by means of fractal geometry. Adv Water Resour 2008;31(1):74–81.
[33] Majumdar A. Role of fractal geometry in the study of thermal phenomena. Ann Rev Heat Transfer 1992;4:51–110.
[34] Gao Y, Wu K, Jiang J. Examination and modeling of fractality for pore-solid structure in cement paste: starting from the mercury intrusion porosimetry test. Construct Build Mater 2016;124:237–43.
[35] ASTM C305-14. Standard practice for mechanical mixing of hydraulic cement pastes and mortars of plastic consistency. West Conshohocken, PA: ASTM International; 2014.
[36] Moukwa M, Atcin PC. The effect of drying on cement pastes pore structure as determined by mercury porosimetry. Cement Concr Res 1988;18(5):745–52.
[37] Aligizaki KK. Pore structure of cement-based materials: testing, interpretation and requirements. London and New York: Taylor & Francis; 2006.
[38] ASTM C1585-13. Standard test method for measurement of rate of absorption of water by hydraulic cement concretes. West Conshohocken, PA: ASTM International; 2004.
[39] Martys NS, Ferraris CF. Capillary transport in mortars and concrete. Cement Concr Res 1997;27(5):747–60.
[40] Pfeifer P, Avnir D. Chemistry in noninteger dimensions between two and three. I. Fractal theory of heterogeneous surfaces. J Chem Phys 1983;79(7):3558–65.
[41] Neimark A. A new approach to the determination of the surface fractal dimension of porous solids. Physica A 1992;191(1–4):258–62.
[42] Purcell WR. Capillary pressures-their measurement using mercury and the calculation of permeability therefrom. J Petrol Technol 1949;1(2):39–48.
[43] Wheatcraft SW, Tyler SW. An explanation of scale-dependent dispersivity in heterogeneous aquifers using concepts of fractal geometry. Water Resour Res 1988;24(4):566–78.
[44] Yu B, Cheng P. A fractal permeability model for bi-dispersed porous media. Int J Heat Mass Tran 2002;45(14):2983–93.
[45] Yu BM, Li JH. A geometry model for tortuosity of flow path in porous media. Chin Phys Lett 2004;21(8):1569–71.
[46] He Z, Cai R, Chen E, Tang S. The investigation of early hydration and pore structure for limestone powder wastes blended cement pastes. Construct Build Mater 2019;229:116923.
[47] Mahamud MM, Menéndez JM, Sarquís PE. CO_2 activation of chars: effect of burn-off on texture and fractal properties. Fuel Process Technol 2014;119:41–51.
[48] Lee GJ, Pyun SI. The effect of pore structures on fractal characteristics of meso/macroporous carbons synthesised using silica template. Carbon 2005;8(43):1804–8.
[49] Monteiro P. Concrete: microstructure, properties, and materials. McGraw-Hill Publishing; 2006.
[50] Mindess S, Young JF, Darwin D. Concrete. 2nd ed. Englewood Cliffs: Prentice-Hall; 2002.
[51] Gao Y, Jing H, Zhou Z. Fractal analysis of pore structures in graphene oxide-carbon nanotube based cementitious pastes under different ultrasonication. Nanotechnol Rev 2019;8(1):107–15.
[52] Zhu J, Zhang R, Zhang Y, He F. The fractal characteristics of pore size distribution in cement-based materials and its effect on gas permeability. Sci Rep 2019;9(1):1–12.
[53] Jennings HM. A model for the microstructure of calcium silicate hydrate in cement paste. Cement Concr Res 2000;30(1):101–16.
[54] Jennings HM. Colloid model of C–S–H and implications to the problem of creep and shrinkage. Mater Struct 2004;37(1):59–70.
[55] Bernard O, Ulm FJ, Lemarchand E. A multiscale micromechanics-hydration model for the early-age elastic properties of cement-based materials. Cement Concr Res 2003;33(9):1293–309.
[56] Yu P, Duan YH, Chen E, Tang SW, Wang XR. Microstructure-based fractal models for heat and mass transport properties of cement paste. Int J Heat Mass Tran 2018;126:432–47.
[57] Zeng Q, Li K, Fen-Chong T, Dangla P. Surface fractal analysis of pore structure of high-volume fly-ash cement pastes. Appl Surf Sci 2010;257(3):762–8.
[58] Kriechbaum M, Degovics G, Tritthart J, Laggner P. Fractal structure of portland cement paste during age hardening analyzed by small-angle X-ray scattering. Prog Colloid & Polum Sci. 1989;79:101–5.
[59] Zeng Q, Luo M, Pang X, Li L, Li K. Surface fractal dimension: an indicator to characterize the microstructure of cement-based porous materials. Appl Surf Sci 2013;282:302–7.
[60] Hansen TC. Physical structure of hardened cement paste. A classical approach. Mater Struct 1986;19(6):423–36.
[61] Schober P, Boer C, Schwarte LA. Correlation coefficients: appropriate use and interpretation. Anesth Analg 2018;126(5):1763–8.
[62] Wang L, Jin M, Wu Y, Zhou Y, Tang S. Hydration, shrinkage, pore structure and fractal dimension of silica fume modified low heat Portland cement-based materials. Construct Build Mater 2021;272:121952.
[63] Jin S, Zhang J, Han S. Fractal analysis of relation between strength and pore structure of hardened mortar. Construct Build Mater 2017;135:1–7.
[64] Zhang Z, Thiery M, Baroghel-Bouny V. Investigation of moisture transport properties of cementitious materials. Cement Concr Res 2016;89:257–68.
[65] Bogner A, Schatz J, Dehn F, Müller HS. Influence of drying on the microstructure of hardened cement paste: a mercury intrusion porosimetry, nitrogen sorption and SAXS study. J Adv Concr Technol 2020;18(3):83–94.
[66] Winslow D, Liu D. The pore structure of paste in concrete. Cement Concr Res 1990;20(2):227–35.

[67] Baroghel-Bouny V. Caractérisation des pâtes de ciment et des bétons-Méthodes, analyse, interpretations. Paris: LCPC Publications; 1994.
[68] Murat M. Stabilité thermique des aluminates de calcium hydratés et phases apparentées. Caractérisation par les méthodes thermoanalytiques. Italy: Aluminates Calcium, Int Semin; 1982. p. 59–84. Turin.
[69] Fu J, Yu Y. Experimental study on pore characteristics and fractal dimension calculation of pore structure of aerated concrete block. Adv Civ Eng 2019;2019.
[70] Abell AB, Willis KL, Lange DA. Mercury intrusion porosimetry and image analysis of cement-based materials. J Colloid Interface Sci 1999;211(1):39–44.
[71] Wood DA. Techniques used to calculate shale fractal dimensions involve uncertainties and imprecisions that require more careful consideration. Adv. Geo-Energy Res. 2021;5(2):153–65.
[72] Wang F, Li S. Determination of the surface fractal dimension for porous media by capillary condensation. Ind Eng Chem Res 1997;36(5):1598–602.